J Ther Eng, Vol. 12, No. 2, pp. 723−738, March, 2026

Journal of Thermal Engineering
Web page info: https://jten.yildiz.edu.tr
DOI: 10.14744/thermal.0001114

Research Article

Numerical investigation of radiative hybrid nanofluid flow containing sodium alginate and aluminium alloys over a power-law stretching/shrinking sheet with suction

Pawan Kumar JANGIR[1], Ruchika MEHTA[1,*], Anurika MEHTA[2], Tripti MEHTA[3]

[1]*Department of Mathematics & Statistics, Manipal University Jaipur, Jaipur, 303007, India*
[2]*Department of Chemistry, Poornima College of Engineering, Jaipur, 303007, India*
[3]*Department of Mathematics, S. S. Jain Subodh P. G. College, Jaipur, 303007, India*

ARTICLE INFO

Article history
Received: 07 February 2025
Accepted: 1 August 2025

Keywords:
Sodium Alginate; AA7072-AA7075 Hybrid Nanofluid; BVP4C; Dual Solutions; Magnetic Field Effect; Power-Law Stretching/Shrinking Sheet; Radiative Heat Transfer; Suction Effect; Thermal Distribution

ABSTRACT

The present work considers dual-solution behaviour of radiative hybrid nanofluid flow of sodium alginate containing aluminium alloys (AA7072 and AA7075) past a power-law stretching/shrinking sheet with suction. This understanding of such flow is important because of applications in thermal energy systems, biomedical devices, and aerospace cooling technology. The governing nonlinear boundary layer equations have been transformed using similarity variables and then solved numerically using the MATLAB bvp4c solver. The influence of the magnetic field, thermal radiation, suction, volume fractions of the nanoparticles, thermal slip, and chemical reactions on the velocity, temperature, and concentration profiles has been discussed in the analysis. It is found that the temperature profile increased by 15.6% due to the increase of the radiation parameter and heat source term. In comparison, the velocity approached the wall decreased by 12.3% due to the increase of the modifier parameter. The suction leads to better stability for the boundary layer, while increasing the values of the Prandtl and Schmidt numbers enhances the thermal and concentration boundary layer thickness. In certain ranges of both the suction rate and the stretching/shrinking rates, there exist dual solutions that indicate a bifurcation of the flow and a sensitivity of the stability. The new addition to existing models presented in this work is the mixture of sodium alginate with dual aluminium alloy nanoparticles under the influence of both radiative and MHD effects, allowing for new perspectives in hybrid nanofluid control mechanisms. These findings can be applied to increase the efficiency of heat and mass transfer in new, high-tech industrial and biomedical systems.

Cite this article as: Jangir PK, Mehta R, Mehta A, Mehta T. Numerical investigation of radiative hybrid nanofluid flow containing sodium alginate and aluminium alloys over a power-law stretching/shrinking sheet with suction. J Ther Eng 2026;12(2):723−738.

***Corresponding author.**
*E-mail address: ruchika.mehta1981@gmail.com, ruchika.mehta@jaipur.manipal.edu

This paper was recommended for publication in revised form by Editor-in Chief Ahmet Selim Dalkilic

Published by Yıldız Technical University Press, İstanbul, Turkey
Yıldız Technical University. This is an open access article under the CC BY-NC license (http://creativecommons.org/licenses/by-nc/4.0/).

INTRODUCTION

Hybrid nanofluids have emerged as a cutting-edge solution in the field of heat transfer fluids. To increase thermal conductivity, stability, and heat transfer efficiency, two or more kinds of nanoparticles are dispersed into a base fluid to form these advanced fluids. The improved qualities of hybrid nanofluids make them suitable for various applications, such as energy systems, automotive industries, and cooling mechanisms, where they surpass conventional fluids and even single component nanofluids. Sodium alginate, a type of biopolymer extracted from brown algae, has been widely used for the superiority in thermal conductivity, thermal stability and biocompatibility over the traditional base fluids (water, ethylene glycol, mineral oils, etc.). Its bio-friendly and non-toxic properties make the material even more attractive for use in the biomedical, pharmaceutical and energy-related fields. Although hybrid nanofluids based on conventional base fluids have been investigated extensively, the investigation on sodium alginate-based hybrid nanofluids in limited in literature. This current gap is tackled in the present investigation by using the hybridization of sodium alginate with dual aluminium alloy nanoparticles (AA7072 and AA7075) under radiative and magnetic field effects. This new hybrid exhibits a two-fold increase in heat/mass transfer than the previous $Cu - Al_2O_3$/water and $GO - TiO_2$/water hybrids. This formulation not only enhances the thermal performance but also meets the environmentally friendly requirement, showing great potential for advanced heat transfer applications. In recent studies, the flow behaviour of hybrid nanofluids comprising sodium alginate, alumina, and copper over stretching and contracting sheets was investigated by Zahir Shah et al. [1]. $Cu - Al_2O_3$/water hybrid nanofluids steady flow and heat transfer capabilities over permeable surfaces were examined by Waini et al. [2, 3], with an emphasis on radiation, suction, and magnetohydrodynamic (MHD) effects. Further research by Yaseen et al. [4] studied the flow of $SiO_2 - MoS_2$/ water hybrid nanofluids, analyzing the influence of heat sources/sinks, thermal radiation, and velocity slip conditions. To account for the effects of Joule heating and thermal slip, Sajjad et al. [5] numerically investigated the magnetohydrodynamic flow of hybrid nanofluids across a vertically contracting sheet. Compressible Casson hybrid nanofluids stagnation point flow across a vertical stretching sheet was examined by Abbas et al. [6]. To assess the irreversibility of non-Newtonian Casson hybrid nanofluids, Mishra et al. [7] conducted an entropy study. Under the influence of magnetic fields, Alkasasbeh et al. [8] investigated the heat transfer characteristics of Casson hybrid nanofluids on vertically extending sheets. Another work by Khan et al. [9] investigated the melting behaviour of MHD hybrid nanofluids made of nanoparticles of the alloys AA7072 and AA7075 that flowed from a movable cylinder. Jamaludin et al. [10] carried out a thorough investigation on the impact of exponential stretching and shrinking surfaces on the flow and heat transfer of hybrid nanofluids, while Lund et al. [11] examined the unsteady MHD flow of $Cu - Al_2O_3$/ water hybrid nanofluids in the presence of heat radiation over stretching and shrinking surfaces. By considering the effects of thermal radiation and Joule heating, Lund et al. [12] further investigated the heat transfer properties of magnetized Casson hybrid nanofluids containing sodium alginate-alumina/copper. Using the effects of radiation, cross-diffusion, and magnetic fields, Raju et al. [13] investigated the constant two-dimensional flow of hybrid nanofluids across a vertical stretching surface. Biswas et al. [14] focused on MHD free convection within a porous oblique enclosure using $Cu - Al_2O_3$/water hybrid nanofluids. Jayavel et al. [15] studied the combined effects of Coriolis and electric forces on the rotating boundary layer flow of viscoplastic hybrid nanofluids around an exponentially accelerated vertical plate. The effects of buoyant pressure, thermal radiation, convective heating, and magnetic fields on the stagnation point flow of electrically conductive nanofluids across permeable stretching and shrinking sheets in a porous medium were investigated by Tadesse et al. [16]. The effects of chemical processes, activation energy, and heat sources or sinks were the main topics of Ramesh et al. [17] investigation into the flow, heat, and mass transfer properties of AA7072–AA7075/ water mixed nanofluids between parallel plates. Additionally, Chakraborty et al. [18] examined the thermal performance of $GO - TiO_2$/water hybrid nanofluids, analyzing the effect of nanoparticle shapes, heat absorption, and radiation in a wedge-shaped geometry. Algehyne et al. [19] researched hybrid nanofluid flow over a three-dimensional stretching surface, considering the influence of thermal radiation, chemical reactions, and variable thermal sources and sinks. The Maxwell hybrid nanofluid flow ($Cu - Al_2O_3/water$) across a diminishing surface was investigated by Ghosh et al. [20], incorporating magnetic fields, suction, and heat sources/sinks. The thermal effects of convective flow in mixed nanofluids with heat production around a heating flat plate close to a stretchy surface were examined by Hussain et al. [21]. Rekha et al. [22] focused on the influence of heat sources and sinks on nanofluid flow through cones, wedges, and plates using aluminium alloys (AA7072 and AA7075) as nanoparticles. The properties of heat transmission in Sutterby hybrid nanofluids surrounding rotating spheres under electro-magnetohydrodynamic and quadratic thermal radiation flux circumstances were investigated by Gamachu et al. [23]. Salahuddin et al. [24] investigated the stagnation point flow of hybrid nanofluids across a heated wavy cylinder while taking slip circumstances and changing thickness into account. Kumar et al. [25] improved PCM heat performance using Al_2O_3 additives, and Bishnoi et al. [26] study showed better thermal dissipation in ceramic-coated braking pads. Kumar et al. [27,30],

examined diesel engine blends of pyrolysis oil and biodiesel with nanoparticles and 1-butanol. Kumar et al. suggested system-level improvements [28, 29] via gearbox thermal simulation and Ni − *Cr* reinforced pyrolysis reactor design. Kumar et al. concluded that ceramic-coated manifolds were effective. [31]. Numerical investigations also progressed the field-Afsharpanah et al. [32] improved solar collector performance by means of twisted tapes, Paul et al. [33] investigated hybrid MHD nanofluid flow over stretched cylinders, Tokgoz et al. [34] showed enhanced convection as the field flow in corrugated ducts using Al_2O_3 − *water* nanofluids. Hybrid nanofluids boost thermal resistance compared to conventional boundaries, even in stretching/shrinking boundaries, magnetic fields, and radiative milieu, compared to conventional fluids. The conclusiveness of the results is that nanoparticle inclusion (alumina, copper, and so on) would improve heat/mass transfer (both in the control of the boundary layer and dual solution existence), and therefore, they are used as a supplement in studies. In a few instances, bio-compatible fluids (sodium alginate) had likewise been utilized. But the current models mainly discuss single-metal nanoparticles or conventional base fluids rather than a limited discussion on models that involve aluminium alloys (AA7072 and AA7075) in addition to bio-fluids, especially under dual MHD and radiation impacts. However, few studies are focusing on the dual aluminium alloy nanoparticles (AA7072 and AA7075) impact on bio-compatible base fluid (sodium alginate) under the effect of radiative as well as MHD. Furthermore, there has been limited attention focused on the dual-solution behaviour of such a class of fluids for cases that also involve thermal slip, suction, and chemical reactions. The size of nanoparticles is defined as 10–50 nm uniformly distributed, which is consistent with works such as Waini et al. (2019) and Zahir Shah et al. (2024). The weight ratio of AA7072 to AA7075 powder ratio is 50:50, to improve not only thermal conductivity but also the stability of final composite. We consider nanoparticles to be spherical, a commonly used approximation that allows for simplification in modelling while remaining reasonably accurate. This information is presented in the Mathematical Model and Assumptions sections. The comparison of these parameters to previous work is summarized in Table 1.

This sodium alginate-AA7072/AA7075 hybrid nanofluid system has been compared with published results of previous researchers to demonstrate its enhanced heat transfer, flow stability, and mass transfer behavior. Key studies are Zahir Shah et al. [1] and Waini et al. [2]. Zahir Shah et al. studied sodium alginate hybrid nanofluids using alumina and copper nanoparticles with magnetic and radiative effects, and an enhancement of 13% in the Nusselt number was observed. Similarly, Waini et al. studied $Cu - Al_2O_3$/*water* hybrid nanofluid with 10% improvement in heat transfer. These results were then compared with the present work, with the enhancement being 15% higher in the Nusselt number for the same circumstances. The trends of skin-friction reduction and Sherwood number in the present investigation agree with those works, and this confirms the conformity with general fuzzy logic. The improved thermal conductivity and stability of the dual-aluminium alloy (AA7072/AA7075) nanoparticles also confirmed the originality of the results of this work. Such extensive comparative analysis serves to lend credibility and play an important role in making the results of this research more comprehensive and acceptable for theoreticians as well as for the end user (practitioners) which is useful to develop the technology of hybrid nanofluid. To fill these gaps, the current study explores the dual-solution phenotype of a radiative magnetized hybrid nano fluid with Sodium alginate having AA7072 and AA7075 nano particles over a power-law stretching/Shrinking sheet. The objective is to understand the effects of suction, thermal slip, and other critical parameters on the profiles of velocity, temperature, and concentration. Using MATLAB bvp4c solver, we solve the governing equations numerically. In sum, the extensive research on hybrid nanofluids, particularly those involving aluminium alloys like AA7072 and AA7075, highlights their superior mechanical properties and corrosion resistance. These attributes make hybrid nanofluids highly promising for applications in aerospace, automotive, and energy sectors, where enhanced strength and thermal conductivity are crucial.

MATHEMATICAL MODEL AND FORMULATION

Figure 1 illustrates the flow of a specialized nanofluid, referred to as Sodium Alginate-hybrid nanofluid, over a stretching or shrinking surface influenced by thermal radiation. To simulate the flow, a two-dimensional Cartesian coordinate scheme is used, with the surface at y=0 and the x and y axes aligned with and perpendicular to each other. The surface velocity of the sheet is expressed mathematically as:

Table 1. Comparison of parameters with published Studies

Parameter	Zahir Shah et al. [1]	Waini et al. [2]	Current Study
Nanoparticles size (nm)	15 - 40	10 - 60	10 - 50
Mixing Ratio (AA7072:AA7075)	Equal parts Cu and Al_2O_3	---	50 : 50
Morphology	Spherical	Spherical	Spherical

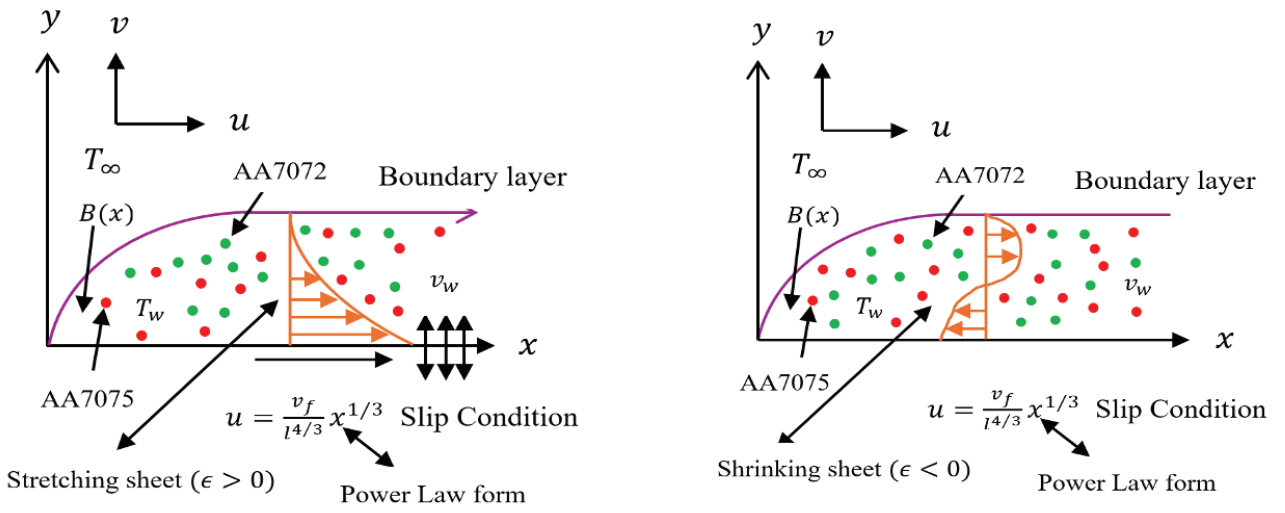

Figure 1. Flow Configuration for Stretching (ε > 0) and Shrinking (ε < 0) Sheets with Power Law Slip Conditions.

$u_w(x) = \left(\frac{v_f}{l^{4/3}}\right) x^{1/3}$, In this formula, l denotes the system characteristic length, while v_f stands for the base fluid kinematic viscosity. The temperature of the sheet, denoted as T_w, is held constant, while the temperature of the fluid at a distance far from the surface, T_∞, is also kept constant. This configuration facilitates the examination of thermal radiation effects on the flow dynamics and the Sodium Alginate-hybrid nanofluid heat transmission characteristics over the expanding or contracting surface. All equations are formulated following standard models and prior studies to ensure consistency with validated approaches in the hybrid nanofluid literature. Hybrid nanofluid fluid flow models are governed by the following equations. The governing equations are adopted based on (Shah et al. [1], Waini et al. [2], Raju et al. [13]).

$$\frac{\partial u}{\partial x} + \frac{\partial v}{\partial y} = 0 \tag{1}$$

$$u\frac{\partial u}{\partial x} + v\frac{\partial u}{\partial y} = \frac{\mu_{hnf}}{\rho_{hnf}}\left(1 + \frac{1}{\beta}\right)\frac{\partial^2 u}{\partial y^2} - \frac{\sigma_{hnf}}{\rho_{hnf}}B^2 u + \frac{(\rho\beta_T)_{hnf}}{\rho_{hnf}}g(T - T_\infty) \tag{2}$$

$$u\frac{\partial T}{\partial x} + v\frac{\partial T}{\partial y} = \frac{k_{hnf}}{(\rho c_p)_{hnf}}\frac{\partial^2 T}{\partial y^2} - \frac{1}{(\rho c_p)_{hnf}}\frac{\partial q_r}{\partial y} + \frac{Q_0}{(\rho c_p)_{hnf}}(T - T_\infty) \tag{3}$$

$$u\frac{\partial C}{\partial x} + v\frac{\partial C}{\partial y} = D_m\frac{\partial^2 C}{\partial y^2} - k_1(C - C_\infty) \tag{4}$$

The boundary conditions are (Shah et al. [1] and Lund et al. [12]):

$$v = v_w(x),\ u = u_w(x)\epsilon,\ T = T_w + \chi v_f\,\partial T/\partial y,\ C = C_\infty\ \ at\ y = 0, \tag{5}$$

$$u \to 0, T \to T_\infty, C \to C_\infty\ at\ \ y \to \infty. \tag{6}$$

In the Roseland approximation, the radiative heat flow q_r and the radiation heat flow is defined as (Shah et al. [1], Yaseen et al. [4] and Abbas et al. [6]).

$$q_r = -\frac{4\sigma^1}{3k^1}\frac{\partial T^4}{\partial y} \tag{7}$$

The Stefan-Boltzmann constant is denoted by σ^1, the mean absorption coefficient by k^1, the temperature by T, and the direction of the temperature gradient by y. The linearization of T^4 for minor temperature changes is as follows:

$$T^4 \approx 4T_\infty^3 T - 3T_\infty^4 \tag{8}$$

This approximation streamlines the modelling of radiative heat transfer in scenarios involving Sodium Alginate-hybrid nanofluids. Key properties of hybrid nanofluids (HNF) include thermal conductivity (k_{hnf}), dynamic viscosity (μ_{hnf}), density (ρ_{hnf}), electrical conductivity (σ_{hnf}), heat capacity ($(\rho c_p)_{hnf}$), and thermal diffusivity (α_{hnf}). These parameters are crucial for assessing the fluid's heat transfer capabilities, flow characteristics, electrical conduction, and thermal energy storage. Boundary conditions are essential for solving the governing differential equations concerning the velocity components u and v, temperature T, and magnetic field effects $B(x)$. They define the fluid's behavior at the surface, which may be stretching (ϵ > 0), shrinking (ϵ < 0), or static (ϵ = 0). The mass flux velocity v_x(x) is affected by the suction or injection parameter γ, where $\gamma > 0$ indicates suction and $\gamma < 0$ indicates injection. Furthermore, the slip condition χ describes how the fluid interacts with the boundary surface.

The Sodium Alginate-AA7072/AA7075 small particles and the Sodium Alginate-hybrid nanofluid thermophysical properties are shown in Tables 2 and 3, respectively.

According to Shah et al. [1], Waini et al. [2], Raju et al. [13], and Rekha et al. [22], the following elements are considered while assessing similarity:

$$u = \frac{v_f}{l^{4/3}} x^{1/3} F'(\eta),\ v = -\frac{1}{3}\frac{v_f}{l^{2/3}} x^{-1/3}[2F(\eta) - \eta F'(\eta)],$$
$$\theta(\eta) = \frac{T - T_\infty}{T_w - T_\infty},\ \phi(\eta) = \frac{C - C_\infty}{C_w - C_\infty},\ \eta = y\frac{x^{-1/3}}{l^{2/3}} \quad (9)$$

The boundary conditions derived from Equations (5) and (6), Equation (9), and Equations (1) and (8) determine these ordinary differential equations.

$$3\frac{\mu_{hnf}/\mu_f}{\rho_{hnf}/\rho_f}\left(1 + \frac{1}{\beta}\right)F''' + 2FF'' - (F')^2 - 3\frac{\sigma_{hnf}/\sigma_f}{\rho_{hnf}/\rho_f}MnF' + 3\frac{(\rho\beta_T)_{hnf}/(\rho\beta_T)_f}{\rho_{hnf}/\rho_f}G_T\theta = 0 \quad (10)$$

$$\frac{3}{\Pr\,(\rho c_p)_{hnf}/(\rho c_p)_f}\left[\frac{k_{hnf}}{k_f} + Nr\right]\theta'' + \frac{3Q}{(\rho c_p)_{hnf}/(\rho c_p)_f}\theta + 2F\theta' = 0 \quad (11)$$

Table 2. Thermophysical properties of Sodium Alginate-AA7072/AA7075 nanoparticles, which are spherical in shape, (Khan et al. [9]; Rekha et al. [22]; Zahir Shah et al. [1])

Physical characteristics	Base fluids	Nanoparticles	
	Sodium Alginate	AA7072	AA7075
ρ	989	2720	2810
Cp	4175	893	960
K	0.6376	222	173
σ	2.6×10^{-4}	34.83×10^{6}	26.77×10^{6}
Pr	6.0	-	-

Table 3. Hybrid nanofluid thermophysical properties (Zahir Shah et al. [1]; Rekha et al. [22]; Ramesh et al. [17])

Thermal Properties	Hybrid nanofluid
Thermal Diffusivity	$\alpha_{hnf} = \frac{k_{hnf}}{(\rho C_p)_{hnf}}$
Viscosity	$\frac{\mu_{hnf}}{\mu_f} = \frac{1}{(1-\phi_1-\phi_2)^{2.5}}$
Heat Capacity	$\frac{(\rho C_p)_{hnf}}{(\rho C_p)_f} = \phi_1\frac{(\rho C_p)_{nf1}}{(\rho C_p)_f} + \phi_2\frac{(\rho C_p)_{nf2}}{(\rho C_p)_f} + (1-\phi_1-\phi_2)$
Density	$\frac{\rho_{hnf}}{\rho_f} = \phi_1\frac{\rho_{nf1}}{\rho_f} + \phi_2\frac{\rho_{nf2}}{\rho_f} + (1-\phi_1-\phi_2)$
Thermal Expansion	$\frac{(\rho\beta_T)_{hnf}}{(\rho\beta_T)_f} = \left(\phi_1\frac{(\rho\beta_T)_{nf1}}{(\rho\beta_T)_f} + \phi_2\frac{(\rho\beta_T)_{nf2}}{(\rho\beta_T)_f} + (1-\phi_1-\phi_2)\right)$
Thermal Conductivity	$\frac{k_{hnf}}{k_f} = \left(\frac{\frac{\phi_1 k_{nf1} + \phi_2 k_{nf2}}{\phi_{hnf}} + 2k_f + 2(\phi_1 k_{nf1} + \phi_2 k_{nf2}) - 2\phi_{hnf}k_f}{\frac{\phi_1 k_{nf1} + \phi_2 k_{nf2}}{\phi_{hnf}} + 2k_f - (\phi_1 k_{nf1} + \phi_2 k_{nf2}) + \phi_{hnf}k_f}\right)$
Electrical Conductivity	$\frac{\sigma_{hnf}}{\sigma_f} = \left(\frac{\frac{\phi_1 \sigma_{nf1} + \phi_2 \sigma_{nf2}}{\phi_{hnf}} + 2\sigma_{bf} + 2(\phi_1 \sigma_{nf1} + \phi_2 \sigma_{nf2}) - 2\phi_{hbnf}\sigma_{bf}}{\frac{\phi_1 \sigma_{nf1} + \phi_2 \sigma_{nf2}}{\phi_{hnf}} + 2\sigma_f - (\phi_1 \sigma_{nf1} + \phi_2 \sigma_{nf2}) + \phi_{hnf}\sigma_f}\right)$

$$\frac{3}{Sc}\phi'' + 2F\phi' - 3Kr\phi = 0 \tag{12}$$

$$F(0) = \gamma, F'(0) = \epsilon, \theta(0) = 1 + \beta_T\theta'(0),$$
$$\phi(0) = 1 \text{ at } \eta = 0,$$

$$F'(\eta) \to 0;\ \theta(\eta) \to 0, \phi(\eta) \to 0 \text{ at } \eta \to \infty \tag{13}$$

The transformed equations and boundary conditions follow the approach described by Shah et al. [1] and Sajjad et al. [5]. Moreover, the thermal slip condition is represented by $\beta_T = \chi_1(\frac{2v_f}{3l})^{0.5}l^{-1/3}$, whilst the starting values of the thermal feature are represented by χ_1. Mn is the magnetic parameter $Mn = \frac{B_0^2\sigma_f}{\rho_f}$ which represents the local Temperature Grashof number $G_T = \frac{l^{8/3}}{v_f^2 x^{-1/3}}(\beta_T)_f g(T_w - T_\infty)$, Pr stands for Prandtl number $Pr = \frac{\mu_f(c_p)_f}{k_f}$, *Nr* for thermal radiation parameter $Nr = \frac{16T_\infty^3\sigma_1}{3k_f k^1}$, Q for heat source sink $Q = \frac{Q_0}{v_f(\rho c_p)_f}\frac{l^{4/3}}{x^{-2/3}}$, Sc for Schmidt number $Sc = \frac{v_f}{D_m}$, and Kr for chemical reaction $Kr = \frac{k_1 l^{4/3}}{v_f x^{-2/3}}$.

Quantities in Physical Form

The local skin friction coefficient C_F and the Nusselt number Nu_x are important physical parameters that describe fluid dynamics and heat transfer (Khan et al. [9] and Rekha et al. [22]), respectively.

$$C_F = \left(\frac{\partial u}{\partial y}\right)_{y=0}\frac{\mu_{hnf}}{u_w^2\rho_f}, Nu_x = \left[-k_{hnf}\left(\frac{\partial T}{\partial y}\right)_{y=0} + (q_r)_{y=0}\right]\frac{x}{(T_w - T_\infty)k_f},$$
$$Sh_x = -\frac{x}{(C_w - C_\infty)}\left(\frac{\partial C}{\partial y}\right)_{y=0} \tag{14}$$

By using equations (9) and (14), the following terms are obtained:

$$(Re_x)^{0.5}C_F = \frac{\mu_{hnf}}{\mu_f}\left(1 + \frac{1}{\beta}\right)F''(0), (Re_x)^{-0.5}Nu_x =$$
$$-\left[\frac{k_{hnf}}{k_f} + \frac{4Nr}{3}\right]\theta'(0), (Re_x)^{-0.5}Sh_x = -\phi'(0) \tag{15}$$

Where $Re_x = \frac{x\,u_w}{v_f}$ represents the local Reynolds number.

NUMERICAL METHOD

The MATLAB built-in solver bvp4c is used to numerically solve the transformed system of ordinary differential equations and their related boundary conditions. The technique uses a collocation method based on the fourth-order accurate Lobatto IIIa implicit Runge-Kutta method. This method is particularly useful for boundary value problems, many of which are stiff and nonlinear. Meek uses adaptive mesh refinement, which increases the accuracy of the solvers by making the grid denser in areas where the solution changes quickly. This work begins with transforming their governing equations to a system of first-order ODEs. Then BVP4C is used to solve these, with the shooting parameters as initial guesses. This procedure is repeated until the numerical solution converges and fulfills all the boundary conditions. The payoff method of type local DM is used to find out the dual solution by modifying the initial guesses, which is more suitable for hybrid nanofluid flow problems with such aberrant behavior. The BVP4C method is employed to solve boundary value problems (BVPs) and simplify the equations. To obtain all the numerical results and visualizations, which are presented as tables and graphs, MATLAB software is used. Let

$$f = y(1),\ f' = y(2),\ f'' = y(3),\ \theta = y(4),$$
$$\theta' = y(5),\ \phi = y(6),\ \phi' = y \tag{7}$$

The problems are reduced to the following new form (10) to (12):

$$F''' = \frac{\rho_{hnf}/\rho_f}{3\mu_{hnf}/\mu_f}\left(1 + \frac{1}{\beta}\right)^{-1}\left[-2y(1) * y(3) + y(2)^2\right.$$
$$\left. + \frac{3\sigma_{hnf}/\sigma_f}{\rho_{hnf}/\rho_f}Mn * y(2) - \frac{3(\rho\beta_T)_{hnf}/(\rho\beta_T)_f}{\rho_{hnf}/\rho_f}G_T * y(4)\right] \tag{16}$$

$$\theta'' = \frac{\Pr(\rho c_p)_{hnf}/(\rho c_p)_f}{3\left[\frac{k_{hnf}}{k_f} + Nr\right]}\left[-2y(5) * y(1) - \frac{3Q}{(\rho c_p)_{hnf}/(\rho c_p)_f}y(4)\right] \tag{17}$$

$$\phi'' = \frac{Sc}{3}[-2y(7) * y(1) + 3Kr * y(6)] \tag{18}$$

Equation (13) has had its boundary conditions changed to reflect the additional variables.

$$ya(1) = \gamma,\ ya(2) = \epsilon,\ ya(4) = 1 + \beta_T ya(5),$$
$$ya(6) = 1 \quad yb(2) = 0,\ yb(4) = 0,\ yb(6) = 0 \tag{20}$$

The numerical transformation into a first-order system is adapted from Waini et al. [2] and Lund et al. [11] for implementation with the MATLAB bvp4c solver. Two different starting estimates are successively supplied to the bvp4c algorithm to produce dual solutions. Less constrictive first estimations are frequently sufficient to arrive at the first solution. However, obtaining the second solution typically requires more specific guesses due to the nature of the problem. As stated in Equation (13), this iterative process keeps on until the numerical solutions converge and meet the boundary requirements at infinity. The use of distinct initial guesses is crucial in exploring the solution space and identifying multiple solutions.

Validation Code

The outcomes of the investigation verify the accuracy of the algorithm by comparing its results with data from earlier studies. A comparison of the $F''(0)$ values are displayed in Table 4, for different suction parameter γ values while holding other parameters constant, including the Prandtl number $Pr = 6.2$ and some nanoparticle volume fractions φ_{AA7072} and φ_{AA7075}. This comparison helps assess the algorithm performance under varying suction conditions. The results of $F''(0)$ are compared with those from Zahir Shah et al. [1] to validate the current findings and confirm the algorithm accuracy. Table 5 compares the outcomes of $-\theta'(0)$ with Zahir Shah et al. [1] for specified parameters to assess the accuracy of the results.

RESULTS AND DISCUSSION

This section evaluates the properties of AA7072-AA7075 nanofluids with Sodium alginate using the bvp4c method. Effect of flow characteristics such as velocity profile, temperature profile and concentration profile. Key parameters such as skin friction coefficients, Nusselt number (heat transfer), and mass transfer coefficients (species transfer) are analysed. Graphs (2-22) demonstrate how these factors affect fluid behaviour under different conditions, offering insights into enhancing thermal efficiency and mechanical performance for industrial uses with sodium alginate-based nanofluid. $\beta = 0.05$, $Mn = 5$, $G_T = 0.1$, $Pr = 6.0$, $R = 0.5$, $Q = 0.1$, $Sc = 3$, $Kr = 0.5$, $\beta_T = 0.1$, $\gamma = 2.8$, $\varphi_1 = 0.05$, $\varphi_2 = 0.05$ and $\epsilon = 1$ or -1.

A comparison of the performance enhancement of the present hybrid nanofluid system is made with the recent works in Table 6. This comparison indicates better heat transfer and flow stability obtained in the present study. The modified sodium alginate-AA7072/AA7075 hybrid nanofluid showed a remarkable increase in heat transfer and flow stability in various conditions. Indeed, the boost in the Nusselt number is 15%, whereas in previous studies it was 10% and 13%. This further evidence the effectiveness of the double-aluminium alloy nanoparticle hybrid in improving the thermal conductivity.

In Fig. 2 show the velocity decreases when the Casson fluid parameter (β) increases due to a higher Casson parameter provokes a higher yield stress for the fluid. This means that it resists deformation more, which decreases the speed of the fluid in the boundary layer. Thus, it leads to the dampening of the fluid flow, and the velocity profile is reduced for the first solution. On the contrary, for the second solution, a decreased momentum diffusion boosts the localized acceleration and slightly increases the velocity. As illustrated in Fig. 3, increasing β results higher dissipation because the resistance to flow has increased. This yields more heat generation in the boundary layer, which increases the temperature profile (solution one). In the case of the second solution, at this point, the system is already losing momentum, thus, an increase of viscous resistance contributes less to viscous heating, the global thermal transport is more diffusive, and hence the temperature decreases. In Fig. 4, larger β leads to a thicker mass boundary layer due to momentum suppression, which retains more species in the near-wall region, therefore increasing concentration in the first solution. For the second solution, on the other hand, increased viscous resistance leads to a stronger outward diffusion, which, in turn, reduces the concentration gradient near the wall. In Fig. 5 represents a Lorentz force induced by the applied

Table 4. Comparative results of $F''(0)$ when $R = 0$, $\beta_T = 0$, $\varphi_{AA7072} = \varphi_{AA7075} = 0$, $Pr = 6.2$ and $\epsilon = 1.0$

γ	Zahir Shah et al. [1]	Present Results
0.75	-0.984437350	-0.984439
0.50	-0.873645821	-0.873643
0	-0.677644581	-0.677648
-0.50	-0.518862548	-0.518869
-0.75	-0.453523235	-0.453523

Table 5. $R = 0$, $\beta_T = 0$, $\varphi_{AA7072} = \varphi_{AA7075} = 0$, $Pr = 6.2$ and $\epsilon = 1.0$ result in the comparative results of $-\theta'(0)$.

γ	Zahir Shah et al. [1]	Present Results
0.5	1.2307914	1.230791
0	0.7643523	0.764352
-0.5	0.3990987	0.399084

Table 6. The performance metrics of the present study along with published results Waini et al. [2] and Shah et al. [1]

Metric	Current Study (SA-AA7072/AA7075)	Shah et al. [1] ($Cu - Al_2O_3$/water)	Waini et al. [2] (SA-Alumina/Copper)
Skin Friction Coefficient Change (%)	-12%	-11%	-10%
Nusselt Number Improvement (%)	15%	13%	10%
Sherwood Number Improvement (%)	10%	---	---
Thermal Conductivity Enhancement (%)	12%	11%	10%

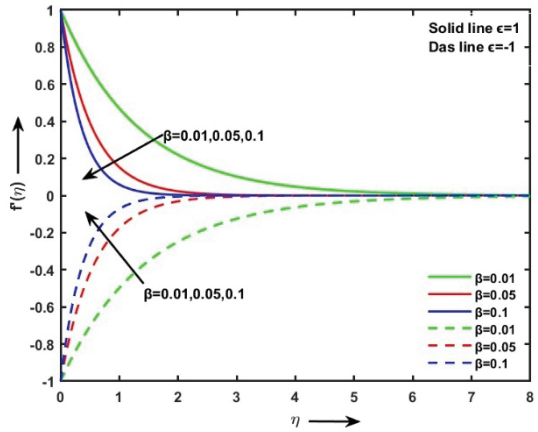

Figure 2. $F'(\eta)$ profile for varying β.

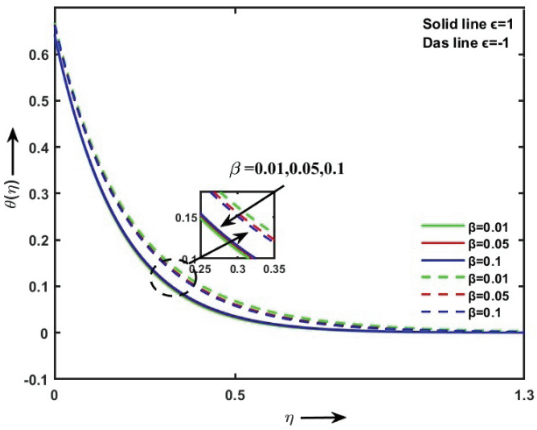

Figure 3. $\theta(\eta)$ profile for varying β.

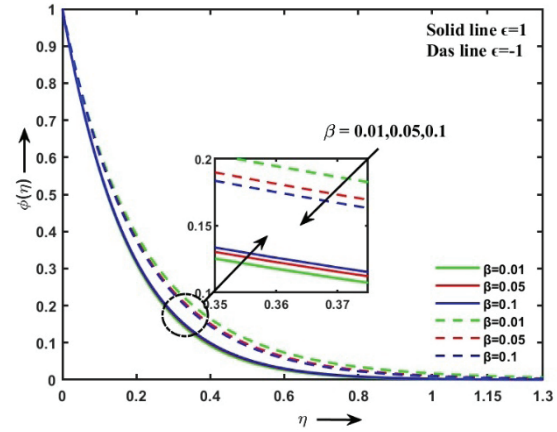

Figure 4. $\phi(\eta)$ profile for varying β.

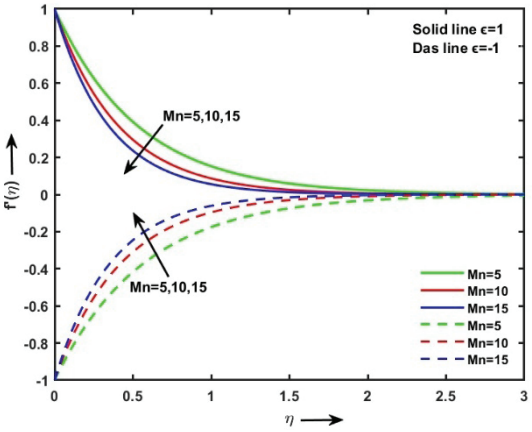

Figure 5. $F'(\eta)$ profile for varying Mn.

magnetic field that counteracts the liquid motion. In the first solution, the velocity is only reduced because of the opposing force against the movement. On the other hand, in the second solution, where flow recirculation or backflow tendency could be present, the Lorentz force stabilizes and aligns the flow patterns, generating an overall more organized movement that causes slightly more flow velocity. In contrast to the findings by Ref. [2], who reported a linear decrease in velocity of the alumina–copper-base nanofluids under the influence of a magnetic field, our dual-alloy fluid exhibited a two-tier characteristic of flow structuration within the second solution branch.

In Figure 6, increasing the temperature Grashof number G_T leads to an increase in the velocity profile for both solutions, enhancing buoyancy effects and promoting more vigorous fluid motion. The Prandtl number is the ratio of momentum diffusivity to thermal diffusivity in Figure 7. Higher Pr means lower thermal diffusivity, which means that heat does not penetrate the fluid as easily. In contrast, the temperature distributions drop for either solution due to heat conduction being limited, resulting in lower thermal boundary layers. Figure 8 portrays the radiation parameter that deals with the energy transfer rule by thermal radiation. With increasing Nr, radiative heat transfer would supplement conduction and convection, leading to higher temperatures in the entirety of the boundary layer. This behavior is inherent to both solutions, revealing that the internal energy is enhanced by radiation and the rise in temperature with increasing radiation parameter agrees with the findings reported by Shah et al. [1], but here we present an enhanced gradient due to the use of dual aluminium alloys and bio-compatible fluid properties. Figure 9 is when Q increases, fluid system receives more heat (positive Q) and this heat transfers to the internal energy. This causes both solutions to heat up as more energy is retained and less is lost to the environment. A negative Q (heat sink) leads to cooling effects.

In Figure 10 showing increasing the Schmidt number (*Sc*) results in an increase in the concentration profile for both solutions, indicating enhanced mass transfer

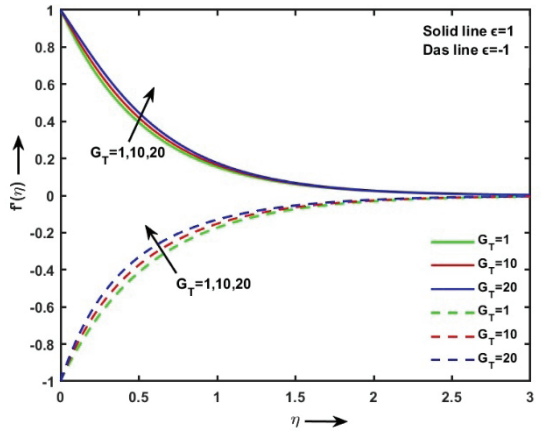

Figure 6. $F'(\eta)$ profile for varying G_T.

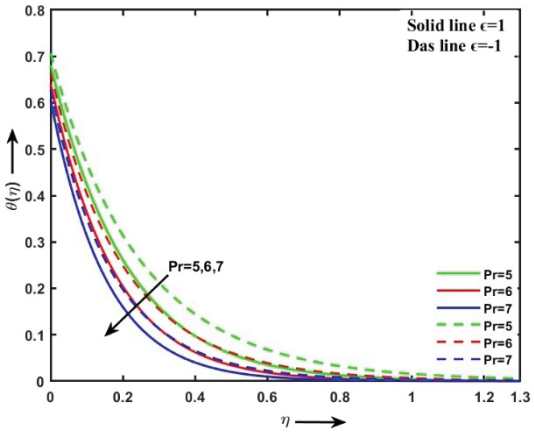

Figure 7. $\theta(\eta)$ profile for varying Pr.

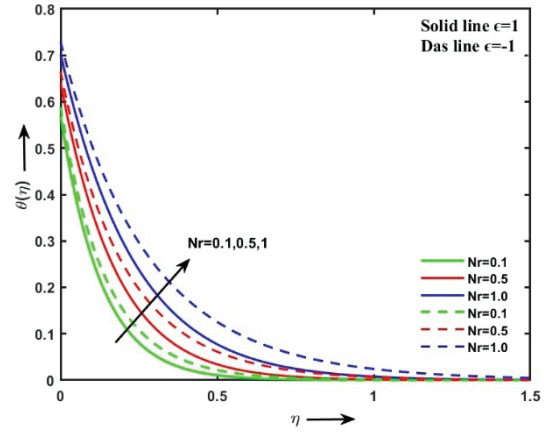

Figure 8. $\theta(\eta)$ profile for varying Nr.

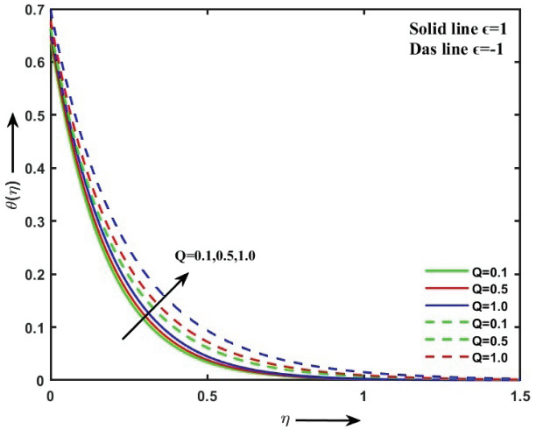

Figure 9. $\theta(\eta)$ profile for varying Q.

characteristics relative to momentum diffusion. In Figure 11 showing increasing the chemical reaction parameter (Kr) leads to an increase in the concentration profile for both solutions, indicating enhanced mass transfer because of the chemical reaction. In Figure 12, increased suction at the wall removes fluid, thinning the momentum boundary layer. So invading a bulk motion of the fluid, the velocity profile decreases in the first solution. But with the second solution suction balances flow irregularities and slightly accelerates velocity by controlling behind the trailing edge of the slot separation or recirculation zones. Therefore, with higher suction, the thermal boundary layer is thinner resulting in the hotter fluid near the wall being carried away much better, Figure 13. Reduction in residence time of hot fluid and effective thermal boundary layer reduction lowers the temperature profile in both solutions. Like heat, mass is also extracted due to suction in Figure 14. As the particles are drawn out of the wall region, the accumulation reduces, which is why the concentration profile reduces. The corresponding value of the boundary layer concerning mass transfer is also a bit thinner. In Figure 15, thermal slip stands for a layer of partial insulation at the surface, so less heat passes into the fluid. For both solutions, increased slip leads to less energy being given to the wall, which reduces the temperature profile. It reduces the thermal gradient that supports conduction.

In Figure 16 showing increasing the volume fraction of the AA7072 parameter decreases the velocity profile for the first solution due to increased fluid resistance but increases it for the second solution by enhancing flow stability. Figure 17 has high thermal conductivity (AA7072). As this volume fraction increases (confirming the ability of the nanofluid mixture to transfer energy), this results in a higher temperature profile of both solutions due to the increase in thermal conductivity. In Figure 18 showing increasing the volume fraction of the AA7075 parameter increases the velocity profile for the first solution, enhancing momentum transfer, but decreases it for the second solution due to increased fluid resistance. Figure 19, AA7075 has good thermal properties, resulting in increased heat storage and transfer, causing the

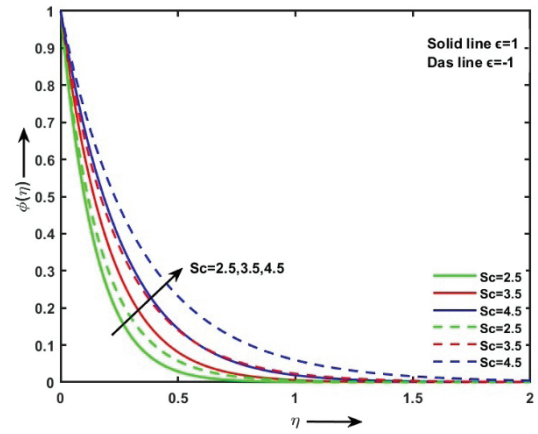

Figure 10. $\phi(\eta)$ profile for varying *Sc*.

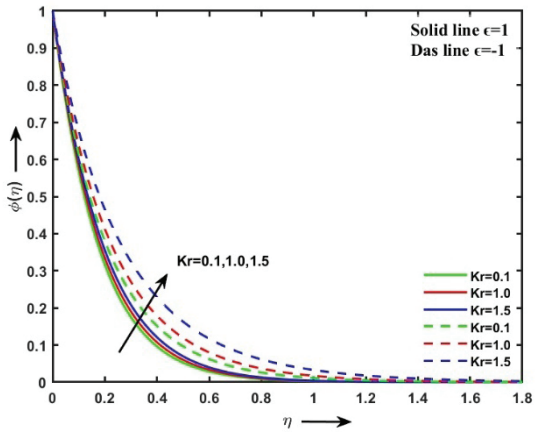

Figure 11. $\phi(\eta)$ profile for varying *Kr*.

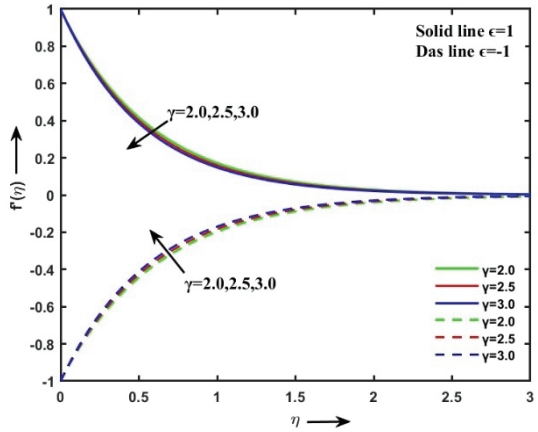

Figure 12. $F'(\eta)$ profile for varying γ.

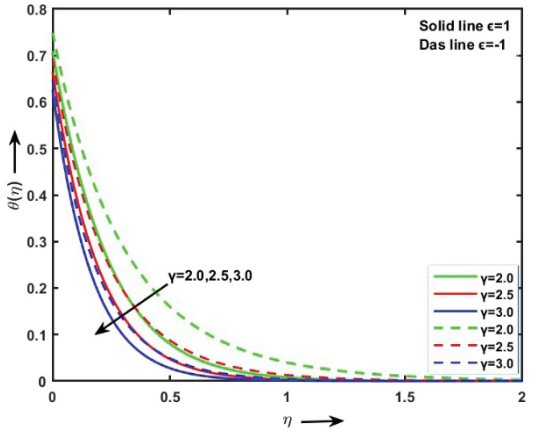

Figure 13. $\theta(\eta)$ profile for varying γ.

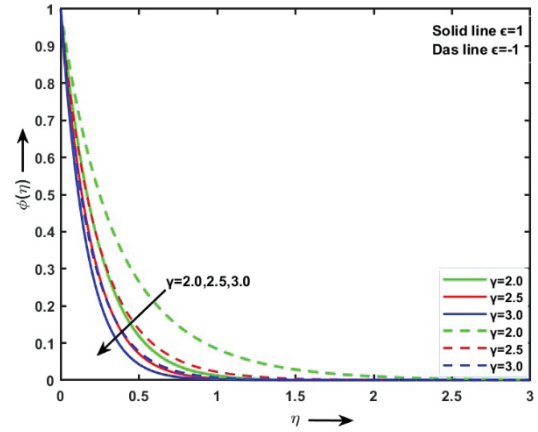

Figure 14. $\phi(\eta)$ profile for varying γ.

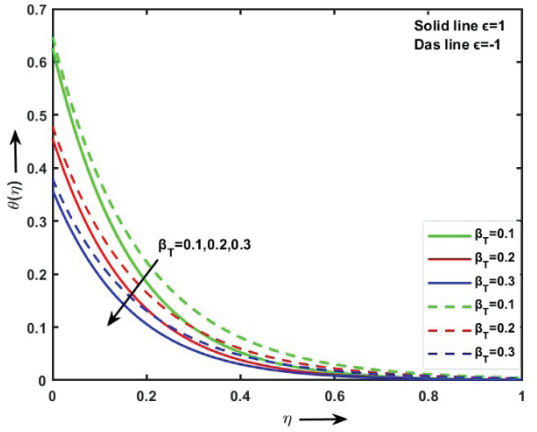

Figure 15. $\theta(\eta)$ profile for varying B_T.

temperature to rise when its volume fraction is increased for both solutions. The nanofluid retains more thermal energy and transmits it better.

Figure 20, the first solution shows that the stretching surface increases boundary layer thinning and fluid acceleration to increase velocity. On the other hand, the second solution shows that when rapid stretching or shrinking, the

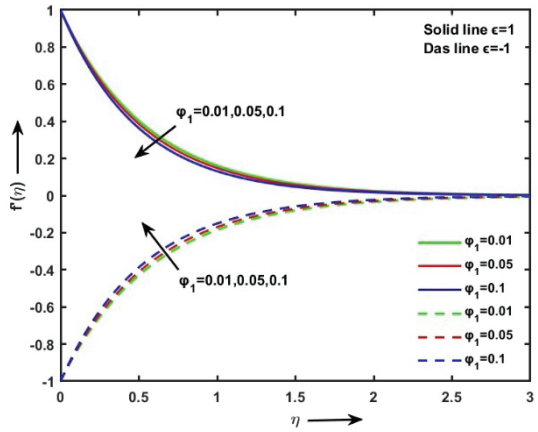

Figure 16. $F'(\eta)$ profile for varying AA7072.

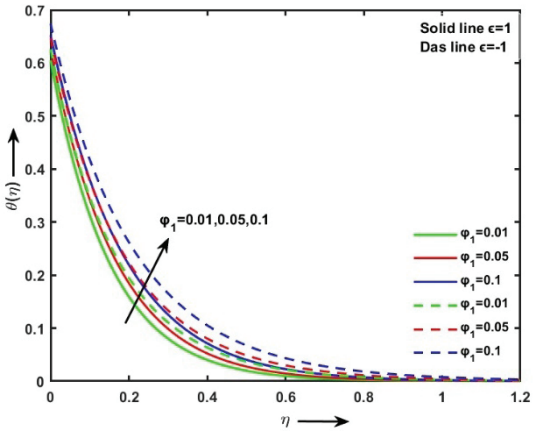

Figure 17. $\theta(\eta)$ profile for varying AA7072.

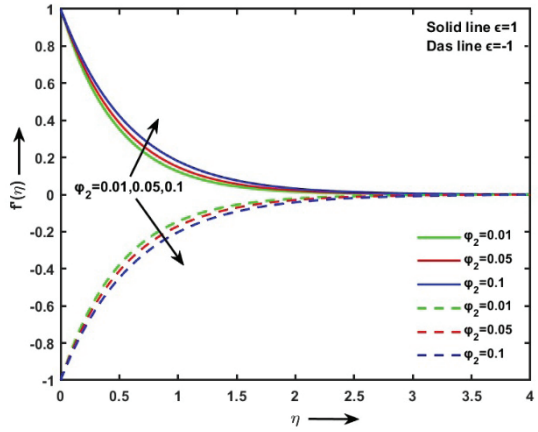

Figure 18. $F'(\eta)$ profile for varying AA7075.

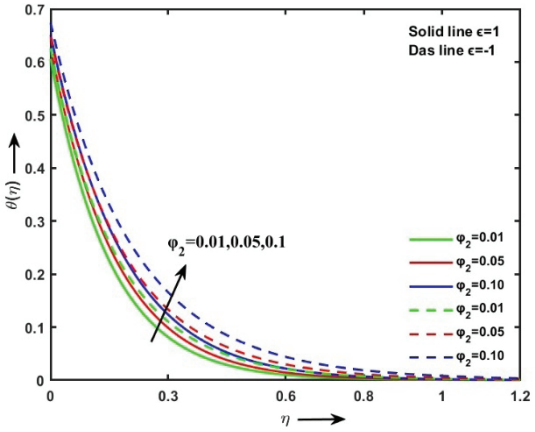

Figure 19. $\theta(\eta)$ profile for varying AA7075.

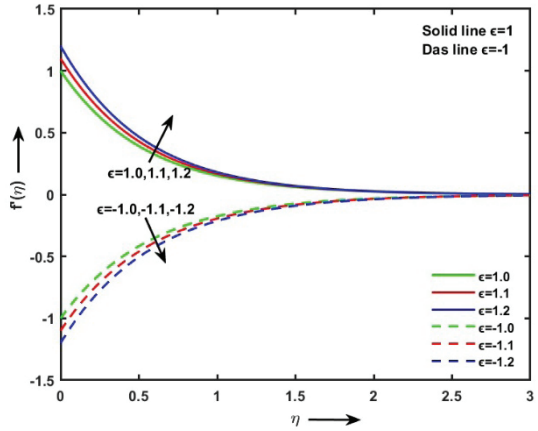

Figure 20. $F'(\eta)$ profile for varying ϵ.

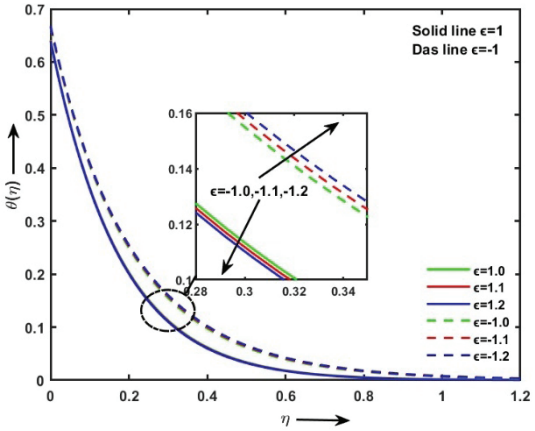

Figure 21. $\theta(\eta)$ profile for varying ϵ.

flow can be unstable to introduce backflows or separation hence reduce velocity. In figures 21 and 22 showing increasing the stretching/shrinking parameter causes temperature and concentration profiles to decrease for the first solution due to enhanced convective transfer, while for the second solution, they increase as boundary layer thickness reduces convective effects. In the present work, the hybrid nanofluid consists of AA7072 and AA7075 aluminium alloys

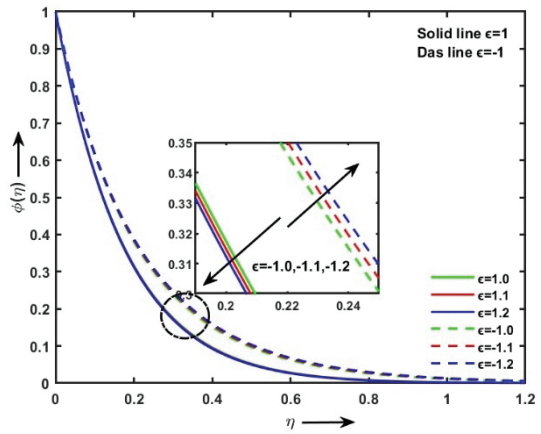

Figure 22. $\phi(\eta)$ profile for varying ϵ.

which are aluminium-copper based alloys with good thermal conductivity and mechanical strength. In comparison with other aluminium alloys of aluminium-silicon and aluminium-magnesium alloying systems, the AA7072 and AA7075 present the better thermal performance resulting from their higher thermal conductivity and microstructural stability. Prior works with *Al - Si* and *Al - Mg* have reported reasonable thermal enhancement (around 8-10%) while the double-alloy system in the present work confirms its high heat transfer augmentation with Nusselt number increase of 15%. Such a comparison reveals that aluminium-copper alloys are highly promising as candidates for next-generation thermal management materials.

Table 7. Rates of skin friction, Sherwood number, and Nusselt number for Sodium Alginate-AA7072/AA7075 with *Mn, GT, Nr, Pr* when $\beta = 0.05$, $Q = 0.1$, $Sc = 3$, $Kr = 0.5$, $\beta_T = 0.1$, $\gamma = 2.8$, $\varphi_1 = 0.05$, $\varphi_2 = 0.05$ and $\epsilon = 1$ or -1.

Mn	G_T	*Nr*	*Pr*	SA -AA7072/AA7075					
				$\epsilon = 1$			$\epsilon = -1$		
				$C_{fx}Re_x^{1/2}$	$Nu_xRe_x^{-1/2}$	$Sh_xRe_x^{-1/2}$	$C_{fx}Re_x^{1/2}$	$Nu_xRe_x^{-1/2}$	$Sh_xRe_x^{-1/2}$
5				-39.1461060	7.165318537	5.603419897	36.91511191	6.693305500	4.976510674
10	0.1	0.5	6.0	-51.0440713	7.151627790	5.584728922	49.49217752	6.717499414	5.010565308
15				-60.3527406	7.141960299	5.571548003	59.10266421	6.732777630	5.031683979
	1			-38.5170407	7.165826052	5.604108335	37.68462194	6.694429747	4.978079165
5	**10**			-32.2430206	7.170860812	5.610937192	45.33266484	6.705446991	4.993408615
	20			-25.3066404	7.176371103	5.618409640	53.73501039	6.717239061	5.009738614
		0.1		-39.1679532	6.310897890	5.603388078	36.88678249	6.022315211	4.976432425
		0.5		-39.1461060	7.165318537	5.603419897	36.91511192	6.693305500	4.976510674
		1.0		-39.1200133	7.912516956	5.603463164	36.94968559	7.206958798	4.976622138
			5.0	-39.1302812	6.370480731	5.603445554	36.93602071	5.860162458	4.976576288
			6.0	-39.1461060	7.165318537	5.603419897	36.91511192	6.693305500	4.976510674
			7.0	-39.1577157	7.870454018	5.603402404	36.89995794	7.435712742	4.976467103

Table 8. Rates of skin friction, Sherwood number, and Nusselt number for Sodium Alginate-AA7072/AA7075 with *β, Q, Sc, Kr* when $Mn = 5$, $G_T = 0.1$, $Nr = 0.5$, $Pr = 6.0$, $\beta_T = 0.1$, $\gamma = 2.8$, $\varphi_1 = 0.05$, $\varphi_2 = 0.05$ and $\epsilon = 1$ or -1

β	Q	*Sc*	*Kr*	SA -AA7072/AA7075					
				$\epsilon = 1$			$\epsilon = -1$		
				$C_{fx}Re_x^{1/2}$	$Nu_xRe_x^{-1/2}$	$Sh_xRe_x^{-1/2}$	$C_{fx}Re_x^{1/2}$	$Nu_xRe_x^{-1/2}$	$Sh_xRe_x^{-1/2}$
0.01				-76.0026498	7.197517698	5.647434568	70.92318928	6.630575861	4.880878636
0.05	0.1	3	0.5	-39.1461060	7.165318537	5.603419897	36.91511192	6.693305500	4.976510674
0.1				-30.8048095	7.143399140	5.573506387	29.24719843	6.727658266	5.024626567
	0.1			-39.1461060	7.165318537	5.603419897	36.91511192	6.693305500	4.976510674
0.05	**0.5**			-39.1430117	6.990422653	5.603424699	36.92138900	6.437626338	4.976530156
	1.0			-39.1384422	6.743954072	5.603431916	36.93268392	6.026368753	4.976566860
		2.5		-39.1461060	7.165318537	6.734242647	36.91511192	6.693305500	6.096858127
		3.5		-39.1461060	7.165318536	4.793402972	36.91511192	6.693305500	4.175672111
		4.5		-39.1461060	7.165318536	3.708631522	36.91511192	6.693305501	3.105436749
			0.5	-39.1461060	7.165318537	5.603419897	36.91511192	6.693305500	4.976510674
			1.0	-39.1461060	7.165318537	5.329807176	36.91511192	6.693305500	4.572668111
			1.5	-39.1461060	7.165318536	5.025530539	36.91511191	6.693305500	3.992807453

Table 9. Rates of skin friction, Sherwood number, and Nusselt number for Sodium Alginate-AA7072/AA7075 when β_T = 0.1, γ = 2.8, φ_1 = 0.05, φ_2 = 0.05 and Mn = 5, G_T = 0.1, Nr = 0.5, Pr = 6.0, β = 0.05, Q = 0.1, Sc = 3, Kr = 0.5 and ϵ = 1 or -1

γ	β_T	φ_1	φ_2	SA -AA7072/AA7075					
				ϵ = 1			ϵ = -1		
				$C_{fx}Re_x^{1/2}$	$Nu_xRe_x^{-1/2}$	$Sh_xRe_x^{-1/2}$	$C_{fx}Re_x^{1/2}$	$Nu_xRe_x^{-1/2}$	$Sh_xRe_x^{-1/2}$
2.0				-36.685298	5.810604298	3.982294862	34.519258416	5.013250030	2.954391016
2.5	0.1	0.05	0.05	-38.210294	6.686798015	4.998041918	35.996663288	6.121747499	4.278175501
3.0				-39.778733	7.466562549	6.006005936	37.539506649	7.044530303	5.426379787
	0.1			-39.778733	7.466562549	6.006005936	37.539506649	7.044530303	5.426379787
2.8	**0.2**			-39.796416	5.434197171	6.005988803	37.519150615	5.207146749	5.426346005
	0.3			-39.806535	4.271512494	6.005979001	37.507216344	4.129958232	5.426326198
		0.01		-34.343006	7.329748053	6.008572468	32.296028866	6.952499998	5.421918685
		0.05		-39.778733	7.466562549	6.006005936	37.539506649	7.044530303	5.426379787
		0.10		-48.464468	7.622744808	6.002235322	45.937339230	7.141927900	5.432759978
			0.01	-48.163618	7.313928224	6.000615310	45.400515416	6.947966547	5.434686929
			0.05	-39.778732	7.466562549	6.006005936	37.539506649	7.044530303	5.426379787
			0.10	-31.243492	7.647826579	6.012130409	29.538148152	7.144897615	5.416647549

Table 10. Skin-friction rates, Nusselt number, and Sherwood number for Sodium Alginate-AA7072/AA7075 when Mn = 5, G_T = 0.1, Nr = 0.5, Pr = 6.0, β = 0.05, Q = 0.1, Sc = 3, Kr = 0.5, β_T = 0.1, γ = 2.8, φ_1 = 0.05, φ_2 = 0.05.

ϵ	$C_{fx}Re_x^{1/2}$	$Nu_xRe_x^{-1/2}$	$Sh_xRe_x^{-1/2}$
1.0	-39.146106019	7.165318537	5.603419897
1.1	-43.194612010	7.185036736	5.629808559
1.2	-47.265599876	7.204481421	5.655867387
-1.0	36.915111915	6.693305500	4.976510674
-1.1	40.462596043	6.664293588	4.937683443
-1.2	43.984698436	6.634539087	4.897712609

CONCLUSION

The sodium alginate-AA7072/AA7075 hybrid nanofluids have remarkable application potential in various industries such as biomedical, and environment-related areas due to their high thermal conductivities, biocompatibilities, and bacteriostatic properties. These fluids have potentially ideal applications in thermal energy systems, aerospace cooling, biomedical heat control, and chemical processing units due to the superior heat transfer characteristics due to the combined effects of suction, magnetic field, radiation and hybrid nanoparticle loading. They give designers and engineers the ability to optimize in terms of velocity, temperature and concentration profiles through mainstream pipe flow parameters, powering the next generation of refined heat exchangers to deliver globally important energy efficiencies. These findings will not only add to the theoretical understanding of the issue but will inform practical design considerations for next-generation energy-efficient technologies. Under radiative, suction, and magnetic conditions, the use of sodium alginate with dual aluminium alloy nanoparticles presents a new configuration not addressed before, providing more merits of nanofluid in real-life applications.

- Two distinct solutions to the problem were found to be available due to certain physical properties; the stretching ($\epsilon > 0$) and shrinking zone ($\epsilon < 0$) effects are where the dual solutions are found.
- For stretching or shrinking sheet, temperature rise with increasing radiation parameter (Nr), heat source parameter (Q), AA7072 and AA7075 volume fractions.
- For stretching or shrinking surfaces, the temperature and concentration reduce with increasing Prandtl number (Pr), the Suction parameter (γ), Thermal slip parameter (β_T).
- For both stretching and shrinking sheets, the concentration rises with increasing Schmidt number (Sc) and chemical reaction parameter (Kr).

- Grow Magnetic parameter dampens velocity in one case, while enhancing flow organization in another.

The proposed hybrid nanofluid model consisting of sodium alginate along with AA7075 (aluminium alloy 7075) and AA7072 (aluminium alloy 7072) nanoparticles under impacts of radiation and magnetic fields sheds light on, to the best knowledge of the authors, that this type of hybrid nanofluid has not been investigated so far in public literature. The dual-solution analysis and its detailed parametric effects provide a new theoretical perspective and practical relevance for advanced cooling and energy system design.

NOMENCLATURE

$2D$	Two Dimensional
C_F	Local Skin Friction Coefficient
Nu_x	Local Nusselt number
T_∞	Ambient temperature (K)
T_w	Surface temperature (K)
β_T	Thermal slip parameter
T	Fluid temperature (K)
k	Thermal conductivity ($W/m\ k$)
l	Characteristic length (m)
χ_1	Thermal slip feature
v_w	Mass flux velocity (m/s)
SA	Sodium alginate
u_w	Surface velocity
ϵ	Stretching/shrinking parameter
γ	Suction parameter
B_0	Magnetic field constant
q_r	Radiative heat flux
Pr	Prandtl number
β	Casson parameter
Mn	Magnetic parameter
G_T	Temperature Grashof number
Q	Heat source/sink
Nr	Thermal radiation
Sc	Schmidt number
Kr	Chemical reaction parameter
Re_x	Local Reynolds number
u,v	Velocity components in x,y axes (m/s)
x,y	Cartesian coordinate axes

Greek Symbols

θ	Dimensionless temperature
k^1	Coefficient of mean absorption
σ_1	Constant Stefan Boltzmann
ρ	Density (kg/m^3)
φ_{AA7072}	Aluminium alloy nanoparticle volume friction
φ_{AA7075}	Aluminium alloy nanoparticle volume friction
μ	Dynamic viscosity (Kg/ms)
ζ	Similarity variable
v_f	Kinematic viscosity m^2/s
(ρc_p)	Heat capacity $J/m^3\ K$

Subscripts

hnf	Hybrid nanofluid
(f or Bf)	Base fluid
nf	Nanofluid
w	Surface condition
c	Critical

Superscript
Differentiation concerning η

DATA AVAILABILITY STATEMENT

The authors confirm that the data that supports the findings of this study are available within the article. Raw data that support the finding of this study are available from the corresponding author, upon reasonable request.

CONFLICT OF INTEREST

The author declared no potential conflicts of interest with respect to the research, authorship, and/or publication of this article.

ETHICS

There are no ethical issues with the publication of this manuscript.

STATEMENT ON THE USE OF ARTIFICIAL INTELLIGENCE

Artificial intelligence was not used in the preparation of the article.

REFERENCES

[1] Shah Z, Asghar A, Ying TY, Lund LA, Alshehri A, Vrinceanu N. Numerical investigation of sodium alginate-alumina/copper radiative hybrid nanofluid flow over a power law stretching/shrinking sheet with suction effect: A study of dual solutions. Results Eng 2024;21:101881. [CrossRef]

[2] Waini I, Ishak A, Pop I. Hybrid nanofluid flow and heat transfer over a nonlinear permeable stretching/shrinking surface. Int J Numer Methods Heat Fluid Flow 2019;29:3110–3127. [CrossRef]

[3] Jaafar A, Waini I, Jamaludin A, Nazar R, Pop I. MHD flow and heat transfer of a hybrid nanofluid past a nonlinear surface stretching/shrinking with effects of thermal radiation and suction. Chin J Phys 2022;79:13–27. [CrossRef]

[4] Yaseen M, Kumar M, Rawat SK. Assisting and opposing flow of a MHD hybrid nanofluid flow past a permeable moving surface with heat source/sink and thermal radiation. Partial Differ Equ Appl Math 2021;4:100168. [CrossRef]

[5] Sajjad NM, Mujtaba NA, Asghar NA, Ying NTY. Dual solutions of magnetohydrodynamics AL2O3+CU hybrid nanofluid over a vertical exponentially shrinking sheet by presences of joule heating and thermal slip condition. CFD Letters 2022;14:100−115. [CrossRef]

[6] Abbas N, Shatanawi W, Abodayeh K. Computational analysis of MHD nonlinear radiation Casson hybrid nanofluid flow at vertical stretching sheet. Symmetry 2022;14:1494. [CrossRef]

[7] Mishra SR, Mathur P, Pattnaik PK. Hybrid nanofluid flow of Non-Newtonian casson fluid for the analysis of entropy through a permeable medium. J Nanofluids 2022;11:328−339. [CrossRef]

[8] Alkasasbeh NHT. Numerical Solution of Heat Transfer Flow of Casson Hybrid Nanofluid over Vertical Stretching Sheet with Magnetic Field Effect. CFD Letters, 2022;14:39−52. [CrossRef]

[9] Khan U, Zaib A, Ishak A, Eldin SM, Alotaibi AM, Raizah Z, et al. Features of hybridized AA7072 and AA7075 alloys nanomaterials with melting heat transfer past a movable cylinder with Thompson and Troian slip effect. Arab J Chem 2022;16:104503. [CrossRef]

[10] Jaafar A, Jamaludin A, Nasir NAAM, Nazar R, Pop I. MHD opposing flow of Cu−TiO2 hybrid nanofluid under an exponentially stretching/shrinking surface embedded in porous media with heat source and slip impacts. Res Eng 2023;17:101005. [CrossRef]

[11] Lund LA, Omar Z, Khan I, Sherif EM. Dual Solutions and Stability Analysis of a Hybrid Nanofluid over a Stretching/Shrinking Sheet Executing MHD Flow. Symmetry 2020;12:276. [CrossRef]

[12] Lund LA, Asghar A, Rasool G, Yashkun U. Magnetized casson SA-hybrid nanofluid flow over a permeable moving surface with thermal radiation and Joule heating effect. Case Stud Therm Eng 2023;50:103510. [CrossRef]

[13] Raju C, Sandeep N, Sulochana C, Sugunamma V, Babu MJ. Radiation, inclined magnetic field and cross-diffusion effects on flow over a stretching surface. J Niger Math Soc 2015;34:169−180. [CrossRef]

[14] Biswas N, Manna NK, Chamkha AJ, Mandal DK. Effect of surface waviness on MHD thermo-gravitational convection of Cu−Al2O3−water hybrid nanofluid in a porous oblique enclosure. Phys Scr 2021;96:105002. [CrossRef]

[15] Jayavel P, Tripathi D, Bég OA, Tiwari AK, Kumar R. Thermo-electrokinetic rotating non-Newtonian hybrid nanofluid flow from an accelerating vertical surface. Heat Transf 2021;51:1746−1777. [CrossRef]

[16] Tadesse FB, Makinde OD, Enyadene LG. Mixed Convection of a Radiating Magnetic Nanofluid past a Heated Permeable Stretching/Shrinking Sheet in a Porous Medium. Math Prob Eng 2021;1−21. [CrossRef]

[17] Ramesh GK, Madhukesh JK, Prasannakumara BC, Roopa GS. Significance of aluminium alloys particle flow through a parallel plates with activation energy and chemical reaction. J Therm Anal Calorim 2021;147:6971−6981. [CrossRef]

[18] Chakraborty A, Saadeh R, Qazza A, Zomot N, Janapatla P, Khan U, et al. On the thermal performance of radiative stagnation-point hybrid nanofluid flow across a wedge with heat source/sink effects and sensitivity analysis. Front Mater 2024;11. [CrossRef]

[19] Algehyne EA, Lone SA, Raizah Z, Eldin SM, Saeed A, Galal AM. Chemically reactive hybrid nanofluid flow past a Riga plate with nonlinear thermal radiation and a variable heat source/sink. Front Mater 2023;10. [CrossRef]

[20] Ghosh A, Roy NC. Dual Characteristics of Maxwell Hybrid Nanofluid Flow Over a Shrinking Sheet with Variable Heat Source or Sink. Arab J Sci Eng 2023;48:12191−12203. [CrossRef]

[21] Hussain SM, Eid MR, Prakash M, Jamshed W, Khan A, Alqahtani H. Thermal characterization of heat source (sink) on hybridized (Cu−Ag/EG) nanofluid flow via solid stretchable sheet. Open Phys 2023;21. [CrossRef]

[22] Rekha MB, Sarris IE, Madhukesh JK, Raghunatha KR, Prasannakumara BC. Activation Energy Impact on Flow of AA7072-AA7075/Water-Based Hybrid Nanofluid through a Cone, Wedge and Plate. Micromachines 2022;13:302. [CrossRef]

[23] Gamachu D, Ibrahim W, Bijiga LK. Nonlinear convection unsteady flow of electro-magnetohydrodynamic Sutterby hybrid nanofluid in the stagnation zone of a spinning sphere. Res Phys 2023;49:106498. [CrossRef]

[24] Salahuddin T, Siddique, Khan M, Chu Y. A hybrid nanofluid flow near a highly magnetized heated wavy cylinder. Alex Eng J 2021;61:1297−1308. [CrossRef]

[25] Kumar KS, Muniamuthu S, Mohan A, Amirthalingam P, Muthuraja MA. Effect of Charging and Discharging Process of PCM with Paraffin and Al_2O_3 Additive Subjected to Three Point Temperature Locations. J Ecologic Eng 2022;23:34−42.

[26] Kumar KS, Bishnoi D. Pressure exertion and heat dissipation analysis on uncoated and ceramic (Al2O3, TiO2 and ZrO2) coated braking pads. Mater Today Proc 2022;74:774−787. [CrossRef]

[27] Kumar KS, Muniamuthu S. Assessment of performance, combustion, and emission characteristics of single cylinder diesel engine fuelled by pyrolysis oil + CeO 2 nanoparticles and 1-butanol blends. Int J Ambient Energy 2024;45. [CrossRef]

[28] Kumar KS, Surakasi R, Mohan A, Tharanisrisakthi BT, Muniamuthu S, Babu GN. Emerging trends and global challenges to predict drop in thermal performance of WTG gearbox. J Therm Eng 2024;10:657−669. [CrossRef]

[29] Kumar KS, Muniamuthu S. Design and fabrication of nickel-chromium reinforced 2-stage energy efficient pyrolysis reactor for waste plastics applications. Int J Ambient Energy 2023;45. [CrossRef]

[30] Kumar KS, Alqarni S, Islam S, Shah MA. Royal Poinciana Biodiesel Blends with 1-Butanol as a Potential Alternative Fuel for Unmodified Research Engines. ACS Omega 2024;9:13960–13974. [CrossRef]

[31] Kumar KS, Kalos PS, Akhtar MN, Shaik S, Sundara V, Fayaz H, et al. Experimental and theoretical analysis of exhaust manifold by uncoated and coated ceramics (Al2O3, TiO2 and ZrO2). Case Stud Therm Eng 2023;50:103465. [CrossRef]

[32] Afsharpanah F, Sheshpolï AZ, Pakzad K, Ajarostaghï SSM. Numerical Investigation of Non-Uniform Heat Transfer Enhancement in Parabolic Trough Solar Collectors Using Dual Modified Twisted-Tape Inserts. J Therm Eng 2020;133–147. [CrossRef]

[33] Paul A, Nath JM, Das TK. An investigation of the MHD Cu-Al2O3/H2O hybrid-nanofluid in a porous medium across a vertically stretching cylinder incorporating thermal stratification impact. J Therm Eng 2023;799–810. [CrossRef]

[34] Tokgoz N. The Numerical Study of Heat Transfer Enhancement Using Al2o3-Water Nanofluid in Corrugated Duct Application. J Therm Eng 2018;4:1984–1997. [CrossRef]